DOI: 10.13009/EUCASS2023-670
Aerospace Europe Conference 2023 – 10TH EUCASS – 9TH CEAS

Cooling system analysis of a clustered module aerospike for upper-stage applications

Alessio Sereno ⋆†, *Matteo Fiore*⋆, *Daniele Bianchi*⋆ *and Francesco Nasuti*⋆
⋆*Sapienza University of Rome*
Via Eudossiana 18, 00184 Rome, Italy
alessio.sereno@uniroma1.it · matteo.fiore@uniroma1.it · daniele.bianchi@uniroma1.it · francesco.nasuti@uniroma1.it
†Corresponding author

Abstract

One of the obstacles in developing annular aerospike nozzles involves effectively managing thermal loads caused by the wide surface area exposed to high heat flux. A modular design is usually proposed as a solution, at the cost of performance reduction. In this framework, the present work focuses on the critical analysis of the design of a regenerative cooling system for a modular aerospike upper-stage LOX/CH4 liquid rocket engine, with a counter-flow cooling circuit fed by methane. Simplified heat transfer models are used to examine channel geometries, and the chosen design is validated through a conjugate heat transfer simulation. Results show that for the present nozzle size a good compromise between thermal management and pressure drop can be obtained, provided that the cooling channels design is suitably realized.

Nomenclature

a	channel height, mm
A	area, m^2
AR	aspect ratio
b	channel width, mm
δp	pressure drop per unit length, bar/m
D_h	hydraulic diameter, m
f	Darcy friction factor
h	convective heat transfer coefficient, $W/(m^2K)$
k	thermal conductivity, $W/(m \cdot K)$
k_s	equivalent sand grain roughness, μm
N	number of channels
p	pressure, bar
P	perimeter, m
q	heat flux, $W/(m^2K)$
$\dot{Q}$	heat transfer rate, W
ρ	density, kg/m^3
R_a	mean roughness, μm
Re	Reynolds number
R_{TC}	thrust chamber radius, m
t	thickness, mm
T	temperature, K
x	axial coordinate, m
z	non-dimensional weight

Subscripts and superscripts

0	stagnation property
aw	adiabatic wall
b	bulk property
c	coolant
co	closeout
DS	Dipprey-Sabersky
g	hot gas
l	liner
r	rib
rad	radiation
w	wall

DOI: 10.13009/EUCASS2023-670

1. Introduction

The increasing competition in the development of space transportation systems necessitates lower launch costs, efficiency, and reliability for current and future launchers. In this framework, aerospike nozzles have emerged as promising candidates due to their unique feature of producing a continuous altitude adaptation up to the design pressure ratio [1, 2, 3, 4, 5], resulting in higher expansion ratios and compactness compared to conventional nozzles [6, 7, 8, 9]. These properties can lead to improved engine specific impulse, ultimately enhancing payload mass fractions. This, in turn, can reduce the size and cost of launch vehicles or increase the payload capacity per mission while maintaining the same amount of propellant.
Since the ideal aerospike can be truncated to a fraction of its full length (typically 20-30%) with only a slight decrease in performance [3, 10], compact designs with very high expansion ratios can be achieved. Concerning the internal expansion part, two main alternatives exist: the annular configuration, in which the central spike is surrounded by a single annular-shaped thrust chamber; the modular configuration, in which the internal expansion is achieved by means of a cluster of conventional bell nozzles arranged circumferentially around the plug [11].
In recent years, there has been a renewed interest in aerospike nozzles [12, 13, 14], supported by advancements in additive layer manufacturing (ALM) techniques. ALM enables the creation of complex shapes and geometries that were previously challenging or impossible to achieve with traditional manufacturing methods [15], and it offers advantages in terms of production costs and time.
Despite the numerous advantages of aerospike nozzles, their implementation in operational launchers has yet to be realized. One of the primary challenges associated with annular aerospike nozzles is the effective management of thermal loads. This challenge arises from the location of the throat in this system, which is situated at the maximum radial distance from the nozzle axis. Consequently, the peak heat flux is distributed over a significantly larger surface area compared to conventional bell nozzles. As a result, a complex cooling system geometry becomes necessary to ensure that the material temperature remains within acceptable limits. However, implementing such a cooling system introduces severe pressure losses [14, 16]. In addition to the high thermal output power, which may exceed the temperature increase limit of the coolants, the large perimeter of the annular aerospike nozzle necessitates a higher number of cooling channels compared to conventional bell nozzles. This leads to a reduction in the mass flow rate available per channel and consequently lowers the heat transfer coefficient of the coolant. In [16], a design for the cooling system of the annular aerospike has been proposed, based on a dual regenerative circuit. As expected, the management of the heat loads proved to be quite challenging, and the main drawback of the system is the large pressure drop in the cooling channels.
In this context, the common envisaged solution is a modular design, which offers significant benefits. For a fixed throat area, utilizing a cluster of modules instead of a single annular thrust chamber results in a smaller perimeter for the throat, see Figure 1. The effect is more evident the higher the expansion ratio of the ideal aerospike. Thus, a modular design facilitates more effective coverage of the thrust chamber perimeter by the cooling channels, making the cooling process less challenging.
In the present work, the analyses are conducted on a 10-ton class LOX/CH4 reference liquid rocket engine for upper-stage applications, for which Nasuti et al. [9] have carried out a design of an aerospike nozzle, based on an ideal contour with an expansion ratio of 280 truncated at 35% of its length. The present work deals with a clustered modules configuration for the same engine. As a first step, the study focuses on the cooling circuit of the modules, while the evaluation of the hot gas side heat transfer for the external expansion plug is left for future works.
In the design of the clustered modular thrust chamber, a balance needs to be found between minimizing the number of units and achieving maximum coverage of the annulus. Restricting the number of modules offers advantages in terms of manufacturing cost, system complexity, and thermal load management. Conversely, maximizing coverage on the annulus reduces performance losses caused by the interaction of supersonic jets. Taking these factors into consideration, a configuration with 42 modules has been arbitrarily selected, and its arrangement is illustrated in Figure 2.
The module, in the following referred to as PME (Plug Module Engine), is a conventional round bell nozzle. The divergent part is shaped as a truncated ideal contour, with an expansion of 30. In line with standard design practice, the combustion chamber has a contraction ratio of 15 and a characteristic length of 1.5 m [17].
The work will be laid out as follows. First, the evaluation of thermal loads by means of computational fluid dynamics simulations of the reactive turbulent hot gas flow in the thrust chamber will be presented. Then, a design methodology based on simplified heat transfer models will be employed to analyze cooling channel geometries and select an appropriate design for the cooling system. Eventually, the selected configuration will be analyzed through a comprehensive conjugate heat transfer simulation, in order validate the effectiveness of the design and to provide a more accurate assessment of the coolant flow characteristics in the channels.

DOI: 10.13009/EUCASS2023-670

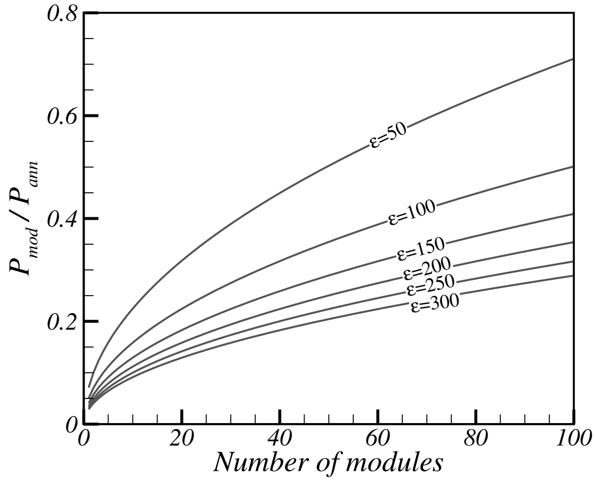

Figure 1: Ratio of the modular to annular configuration throat perimeter, as a function of the number of modules and ideal spike expansion ratio.

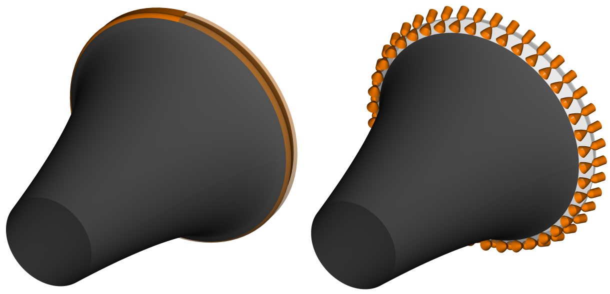

Figure 2: Left: annular plug nozzle. Right: arrangement of the modules on the external expansion section.

2. Evaluation of thermal loads

Starting point for the cooling system design is the evaluation of the heat loads. To accomplish this, simulations of the hot gas flow within the thrust chamber are conducted. The Reynolds Averaged Navier Stokes equations are solved using an in-house finite volume CFD code. Turbulence closure is achieved by employing the Spalart-Allmaras one equation model [18].

Figure 3 illustrates the axisymmetric domain and computational mesh used for simulations on the hot gas side, along with the boundary conditions setup. The combustion products are injected in chemical equilibrium along the left boundary. The equilibrium composition is computed for a pressure of 60 bar and O/F of 2.8, values inspired by Nasuti et al. [9].

Finite rate chemistry is incorporated to evaluate the impact of recombination reactions within the boundary layer on the wall heat flux. The selected kinetic mechanism for this assessment is JL-R (Jones-Lindstedt and Recombination), including 9 species and 7 reactions [19]. The JL-R extends the Jones-Lindstedt global mechanism for hydrocarbon combustion (4 reactions) [20] with 3 recombination reactions, to properly describe the chemical kinetics within the boundary layer. Furthermore, the gas radiation heat flux is modeled with the Discrete Transfer Method [21]. Analogue numerical setups have shown good agreement with heat transfer experimental data of CH4/LOX subscale engines [19, 22, 23].

For convective heat transfer, isothermal and adiabatic wall CFD simulations are exploited to compute the heat transfer coefficient distribution along the wall, which is shown in Figure 4. The heat transfer coefficient is preferred to the wall heat flux, due to its weak dependence on the wall temperature, which is in principle unknown. In the isothermal simulation, the wall temperature is set at 800 K, which is considered a safe operational temperature for ALM copper-based alloys like C-18150 [24, 25]. For what concerns radiation, the gas is modeled as a gray body. The radiation heat flux distribution is also reported in Figure 4. It is important to note that employing combustion products in chemical equilibrium for injection leads to a significant overestimation of both convective and radiation heat flux. In particular it results in a local peak of convective heat transfer in the vicinity of the injector plate as the boundary layer develops [23], which is not expected if the phenomenon of injection and combustion is correctly modeled. However, according to [23], for the present preliminary estimations these simplifying assumptions are deemed more than acceptable since they are expected to affect marginally the heat flux evolution along most of the surface wetted by the hot gas, starting from the beginning of the convergent section.

3. Cooling system

The baseline configuration selected here for the cooling system of the modules involves a counter-flow regenerative circuit fed by methane, flowing in rectangular cross section cooling channels. The total available CH4 mass flow rate is 7.3 kg/s (0.174 kg/s per module). The primary goal of the design is to ensure that the wall temperature remains below the target value of 800 K. To achieve this, the cooling channel geometry will be devised using a simplified heat

DOI: 10.13009/EUCASS2023-670

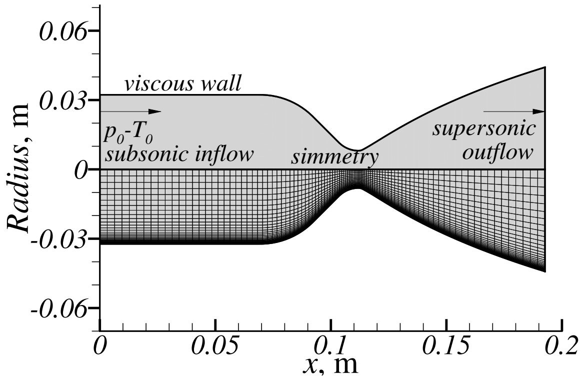

Figure 3: Geometry and computational setup for the PME hot gas side simulations.

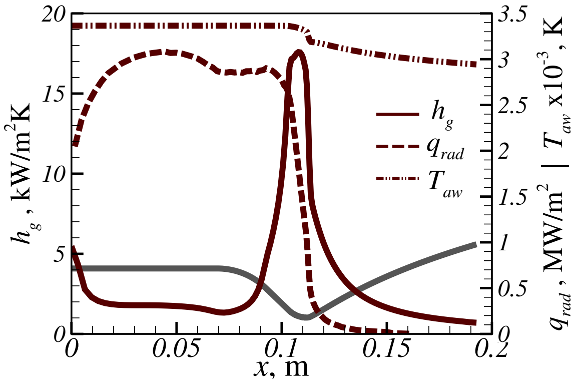

Figure 4: Hot gas side heat transfer coefficient and radiation heat flux for the PME.

transfer model that examines the problem of heat transfer from the hot gas side to the coolant in a one-dimensional fashion, enabling an analytical solution. This conventional approach, which also relies on correlation recently proposed in literature, allows for quick analysis of a large number of different configurations. Subsequently, the selected channel design will be validated for its cooling efficiency through a comprehensive conjugate heat transfer simulation.

3.1 Coolant budget

The coolant budget is computed as the primary step of the regenerative cooling system, to assess if the coolant is enough to cool down the thrust chamber walls. From the hot gas side inputs (Figure 4), assuming isothermal wall, the resulting heat flux can be integrated along the thrust chamber wall:

$$\dot{Q} = \int_w q dA = \int_w \left[h_g (T_{aw} - T_{w,g}) + q_{rad} \right] dA \tag{1}$$

Assuming that the entire heat is absorbed by the coolant, the coolant enthalpy increase can be computed. Eventually, from the variation in enthalpy, the corresponding rise in bulk temperature, T_b, can be obtained. The necessary thermophysical properties of CH4 for this computation are evaluated through the CoolProp library [26]. The initial temperature of the coolant at the channel inlet is assumed to be 120 K, while a fixed value of pressure (100 bar) is assumed to calculate the temperature corresponding to the evolving bulk enthalpy.

In a parametric analysis obtained assuming different wall temperatures, the resulting heat from Equation 1 allows to get an estimation of the evolution of the coolant bulk temperature in the cooling channels, which is shown in Figure 5. It is observed that lower wall temperatures correspond to higher heat fluxes and thus higher increase in the coolant temperature. To ensure the proper operation of the cooling system, it is crucial that T_b remains below the maximum allowed wall temperature throughout the channel until the outlet, otherwise heat exchange from the wall to the coolant would be impossible. In the present case, even for a relatively low temperature of 600 K, the coolant power budget is satisfied since the bulk temperature at the channels exit is still lower than the wall temperature. Therefore, the design of a cooling circuit fed by the available fuel mass flow rate can be carried out.

3.2 Reduced model for designing the channels geometry

Referring to the channel section depicted in Figure 6, which is obtained by slicing the cooling jacket at a constant x coordinate, the channel geometry can be characterized by three independent parameters: number of channels, N, hydraulic diameter, D_h and aspect ratio, AR. These parameters serve as the basis for calculating the remaining dimensions, as reported in Equation 2.

$$b = \frac{D_h}{2AR}(1 + AR), \quad a = \frac{D_h}{2}(1 + AR), \quad t_r = \frac{2\pi(R_{tc} + t_l)}{N} - \frac{D_h}{2AR}(1 + AR) \tag{2}$$

while the liner and close-out thicknesses t_l and t_{co} can be arbitrarily set. Assuming that heat transfer in the axial direction is negligible, and establishing boundary conditions for both the coolant side and the hot gas side, the sample cross section shown in Figure 6 serves as a reduced computational domain where wall temperatures can be calculated.

DOI: 10.13009/EUCASS2023-670

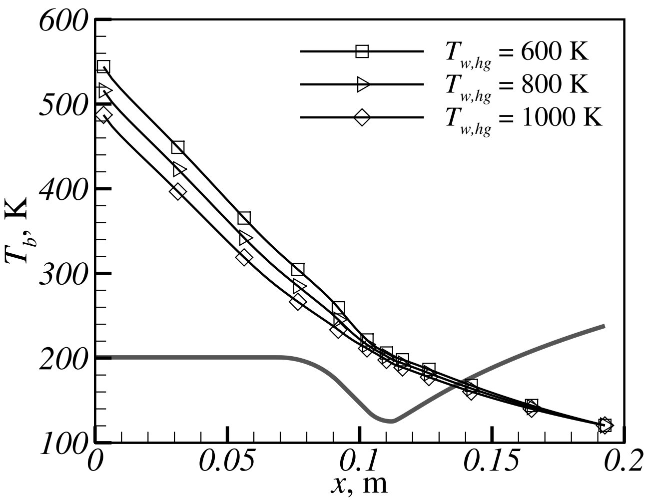

Figure 5: Bulk temperature distribution.

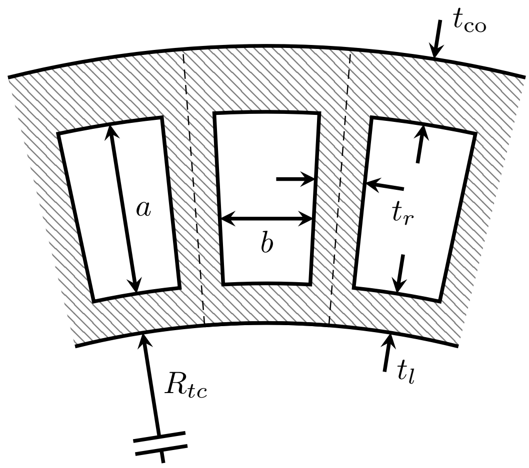

Figure 6: Schematic of the cooling channels section.

For the hot gas side, the boundary condition is that of convective heat transfer and radiation from Section 2, shown in Figure 4. On the coolant side, among the trends for T_b depicted in Figure 5, that for a wall temperature of 800 K is assumed. The convective heat transfer coefficient is evaluated through the correlation of Dipprey and Sabersky [27] for developed, turbulent flow in rough pipes. Additionally, corrections for property change in the boundary layer [28] and channel curvature [29] are considered, and the overall equation for the coolant convective heat transfer coefficient evaluation is reported in Eq. (3).

$$h_c = h_{c,DS} \left(\frac{T_{w,c}}{T_b}\right)^{0.45} \left[Re\left(\frac{D_h}{2R_c}\right)^2\right]^{\pm 0.05} \tag{3}$$

Once the channel section geometry and boundary conditions are set, the method presented by Fagherazzi et al. [30] can be utilized to compute the wall temperature on the hot gas side. This method enables the analytical evaluation of wall temperatures using a simplified 1D theory for the heat transfer modeling in the liner, closeout and rib. The input data are the geometry of the channel, the thermal conductivity of the material, the hot gas and coolant heat transfer coefficients h_g and h_c, reference temperatures T_{aw} and T_b, and radiation heat flux. The hot gas side and coolant side wall temperatures can be then computed using the equations presented in [30], rearranged to take into account the radiation heat flux.

This setup facilitates the exploration of the parameter space, allowing for the prompt association of each geometry triplet (N, D_h, AR) with its corresponding wall temperature, and assess its cooling effectiveness. Additionally, other relevant quantities can be computed. For instance, the pressure drop per unit length is given by Equation 4:

$$\delta p = \frac{1}{2}\rho_b u_b^2 \frac{f}{D_h} \tag{4}$$

where the Darcy friction factor is calculated through the Colebrook and White equation. An evaluation of the equivalent sand grain roughness, needed for both the Colebrook equation and the correlation of Dipprey and Sabersky, is provided by the correlation derived by Stimpson in [31], which relates the equivalent surface roughness to the arithmetic mean roughness R_a. The correlation is reported in Equation 5.

$$\frac{k_s}{D_h} = 18\frac{R_a}{D_h} - 0.05 \tag{5}$$

In the same study, values of R_a ranging from 10 to 14 μm are reported for additively manufactured channels. Therefore, a conservative estimate of $R_a = 14\,\mu m$ is adopted for the present work.

Furthermore, an indicator of the mass of the cooling jacket is also taken into account. The mass per unit length of the ribs can be computed and non-dimensionalized with the mass per unit length of the liner and closeout. Assuming a single material for the cooling jacket, the resulting parameter z is defined in Equation 6.

DOI: 10.13009/EUCASS2023-670

$$z = \frac{A_r}{A_l + A_{co}}$$
$$A_r = N\,a\,t_r\,,\quad A_l = \pi[(R_{TC} + t_l)^2 - R_{TC}^2]\,,\quad A_{co} = \pi[(R_{TC} + t_l + a + t_{co})^2 - (R_{TC} + t_l + a)^2] \tag{6}$$

Such a reduced model allows for the creation of a design map incorporating all the aforementioned information. An example is provided in Figure 7 for the cooling channel section in the throat region. Two $D_h - N$ planes are drawn for $AR = 1$ and $AR = 2$. Gray shaded regions indicate areas where the geometry is deemed inadmissible. For the purpose of this study, geometrical limits are adopted from the work of Fagherazzi et al. on a 3D printed regenerative cooled nozzle [32] and defined as 0.8 mm for the minimum printable thickness, 0.5 mm for the minimum channel width and 8 for the maximum aspect ratio. Isolines of rib thickness, wall temperature, pressure drop per unit length and non-dimensional mass are drawn. This visualization allows to identify practical design criteria. For instance, given the desired wall temperature, minimum pressure drop and minimum non-dimensional mass solutions are found along the minimum rib thickness contour line. Moreover, thanks to the high conductivity of the copper alloy, increasing the aspect ratio of the channels is advantageous for the pressure drop, as the number of channels can be increased and the ribs act as effective cooling fins; however, a trade-off is required as the cooling jacket mass also increases with the aspect ratio.

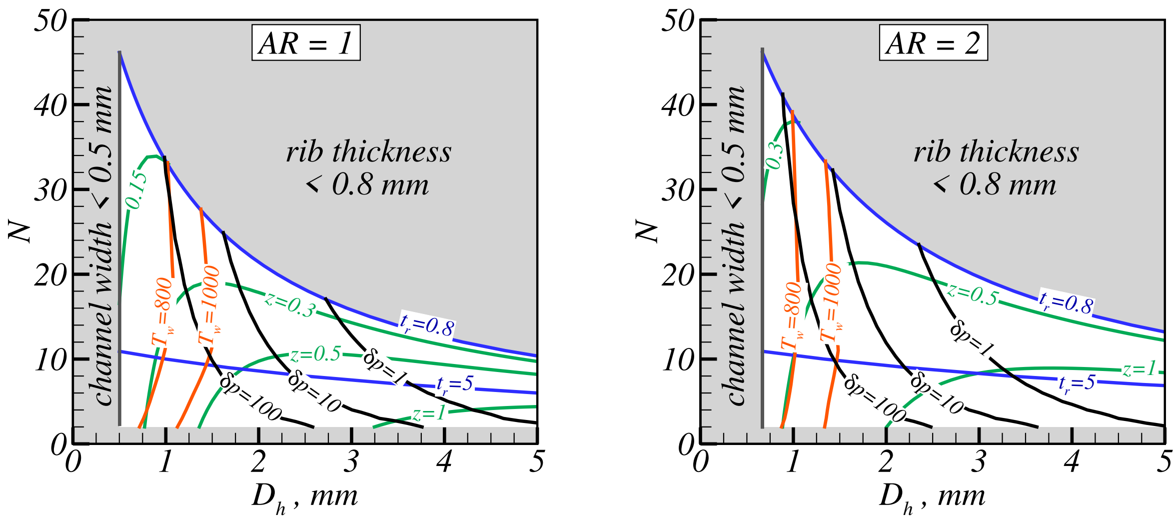

(a) $AR = 1$. (b) $AR = 2$.

Figure 7: Design maps for the channel section.

To initiate the design process, the throat region is identified as the crucial area, as the cooling system needs to withstand the highest heat flux. In Figure 8(a), a design map is presented, focusing on the location where the heat transfer coefficient on the hot gas side reaches its peak. By assuming an aspect ratio of 1.5, the configuration with 36 channels is determined by identifying the intersection between the contour line representing the maximum temperature (800 K) and the minimum rib thickness. Increasing the aspect ratio up to 3, which is the maximum limit for the minimum channel width, effectively reduces the pressure drop. However, this increase in aspect ratio from 1.5 to 3 results in a 25% decrease in pressure drop but a 60% increase in the weight parameter. Consequently, the configuration with the lower aspect ratio of 1.5 is chosen to minimize the number of channels, overall height, and ultimately, the weight parameter.

In order to determine the geometric parameters of the channels in points other than the throat, two constraints are enforced: same number of channels and wall temperature below the maximum target value of 800 K. An example is presented in Figure 8(b), in which the design map is drawn in the plane $D_h - AR$, while N is fixed at 36. Figure 8(b) focuses on a location near the inflow boundary, just ahead the initial convective heat transfer peak. At that location, the perimeter to be covered is much larger with respect to the throat region (since the radius is higher), leading to low aspect ratio channels; therefore, a rib thickness of 2 mm is selected to obtain an aspect ratio of 0.3. Similar criteria are used to design the channels geometry in other locations (7 in total). To obtain the geometry along the entire chamber, the channel height and rib thickness are interpolated between the designed points. The channel width is computed from the local chamber radius, the number of channels, and the rib thickness. The resulting axial evolution of channel

DOI: 10.13009/EUCASS2023-670

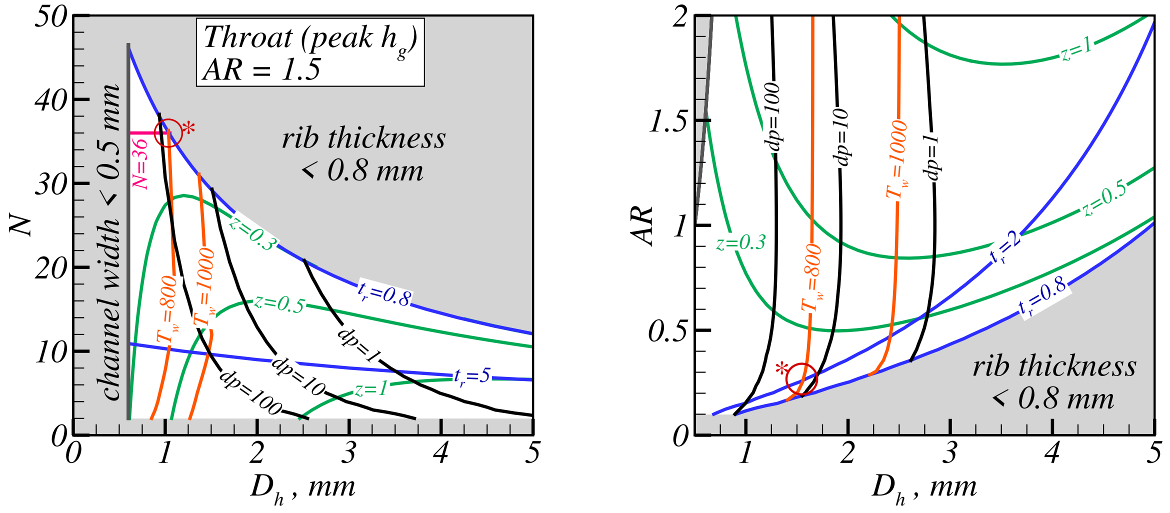

(a) Throat section.

(b) Initial segment of the cylinder.

Figure 8: Design maps. Selected geometries are highlighted by a red circle with a star.

geometrical parameters is illustrated in Figure 9, namely the channel width and height, rib thickness and aspect ratio. Additionally, the liner and close-out thicknesses t_l and t_{co} are set at constant values of 0.8 mm and 1.5 mm, respectively.

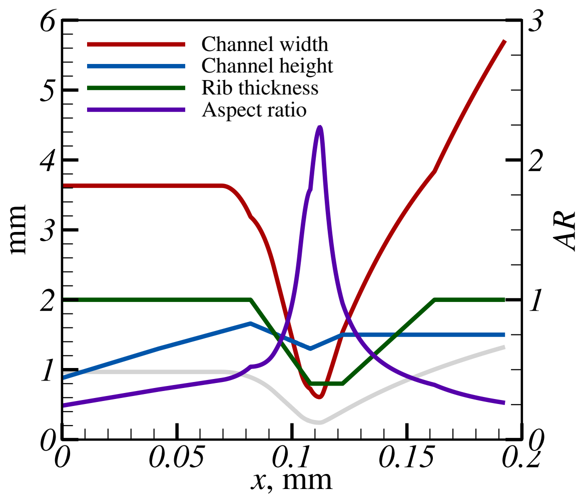

Figure 9: Geometry of the cooling channel.

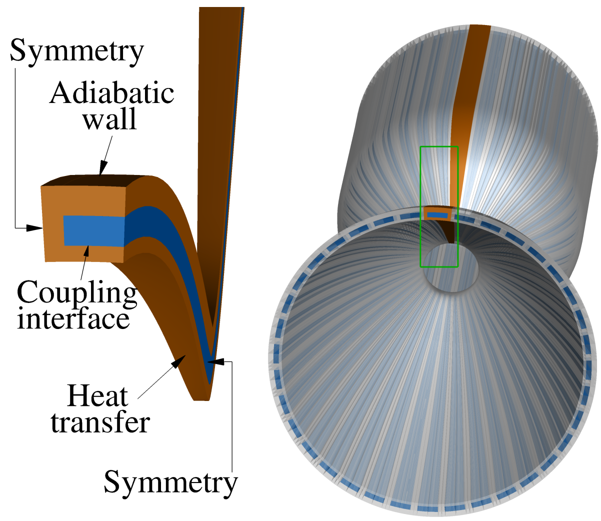

Figure 10: Computational setup and boundary conditions.

4. Conjugate Heat Transfer

4.1 Numerical setup

A conjugate heat transfer approach is utilized to conduct a detailed analysis of the flow and wall temperature in the cooling system. This approach involves the simultaneous integration of the Navier-Stokes equations for the coolant flow and Fourier's law of conduction for heat transfer within the solid material [33]. The flow solver used in this study is an in-house code that integrates the Reynolds Averaged Navier-Stokes equations in conservation form. It employs a second-order accurate Godunov-type finite volume scheme for spatial discretization, and is capable to handle any compressible fluid whose behavior can be represented by a generic equation of state, as fluid properties are stored

DOI: 10.13009/EUCASS2023-670

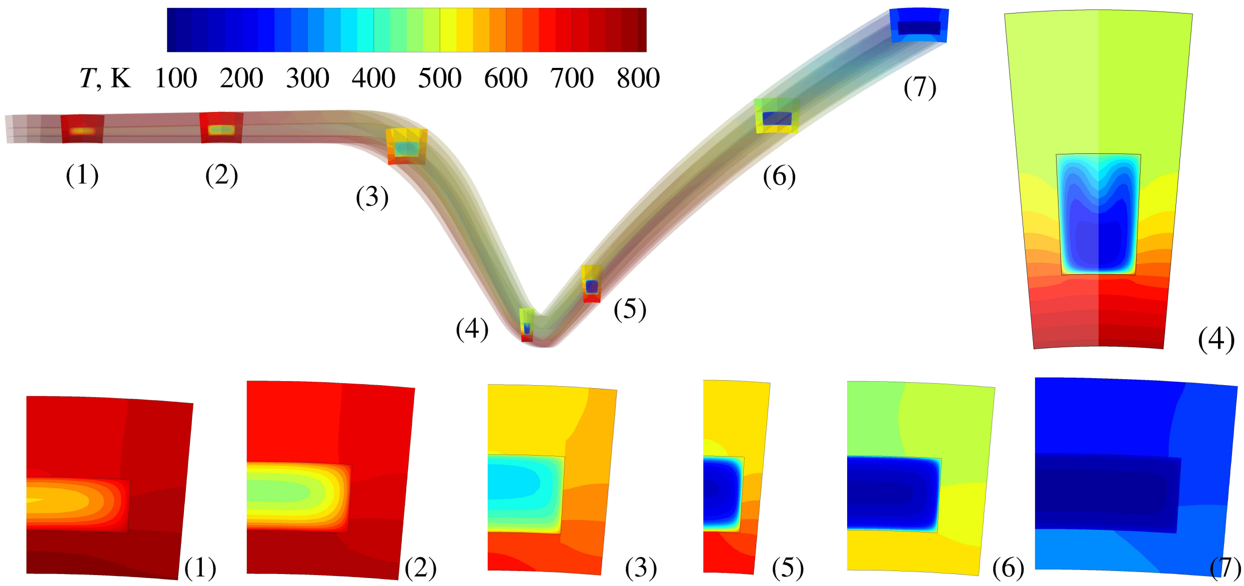

Figure 11: Conjugate heat transfer solution of the cooling channel, highlighting slices at design locations.

in a look-up table. In this study, look-up tables for methane have been generated using the CoolProp library [26]. Turbulence closure is achieved using the one-equation Spalart-Allmaras model [34], extended by Boeing to account for wall roughness [35]. The accuracy of the coolant flow solver has been validated by comparing its results with available experimental data on supercritical nitrogen [36] and transcritical hydrogen [37].

To achieve a coupled solution of the coolant flow and wall heat conduction, an iterative procedure is employed. The wall temperature is enforced at the interface boundaries of both solvers. At each coupling iteration, the coupling algorithm calculates the necessary variation of wall temperature for each cell along the interface to ensure consistent heat flux exchange. This iterative process continues until the maximum temperature variation between two consecutive iterations is sufficiently low and the overall power exchanged reaches a stationary value.

Figure 10 illustrates the computational domain used in this study. To minimize computational effort, the smallest repeatable unit is employed, with symmetric boundary conditions applied to the lateral sides. In the present case, the smallest unit consists of half a channel.

For what concerns the boundary conditions, the inflow for the coolant is defined by enforcing the static temperature (120 K) and mass flow rate, while static pressure (100 bar) is prescribed at the outlet of the channel. For the solid domain, convective heat transfer and radiative heat flux reported in Figure 4 are enforced on the hot gas side, as detailed in Section 2. The external close-out (top side) of the solid is assumed adiabatic.

4.2 Results

The temperature field resulting from the conjugate heat transfer simulation is shown in Figure 11, which displays slices obtained at a constant x coordinate in the design sections. In section (4), the temperature contour exhibits a V-shape, which is a consequence of the secondary motion caused by the channel curvature in the throat, known as Dean vortices [38]. The structure of this secondary motion is illustrated in Figure 12, which shows the pattern of tangential velocity components in the channel cross section in the throat region. The formation of Dean vortices is a result of centrifugal and pressure gradient forces acting on the fluid as it flows through the curved segment of the cooling channel. As the fluid moves along the curved path, the centrifugal force causes the fluid to move away from the inner-radius wall towards the outer-radius wall. The fluid accumulates near the outer wall of the bend, and the centrifugal force acts as a pressure gradient, leading to a non-uniform pressure distribution in the cross section, as shown in Figure 12. The radial pressure gradient leads to the formation of two counter-rotating cells. As a result, an heat transfer enhancement occurs due to the presence of the fluid recirculation in the channel cross section.

Figure 13(a) presents the axial variations of wall temperature and heat flux on the hot gas side. It is immediately apparent that the wall temperature tends to be underestimated before the throat (points 5-7) and overestimated after the throat (points 1-3). This discrepancy can be attributed to errors in predicting the convective heat transfer coefficient of the coolant using Equation 3, as the correlation fails to capture the complex three-dimensional behavior of the fluid. The largest disagreement between the reduced model and the conjugate heat transfer simulation is observed at point

DOI: 10.13009/EUCASS2023-670

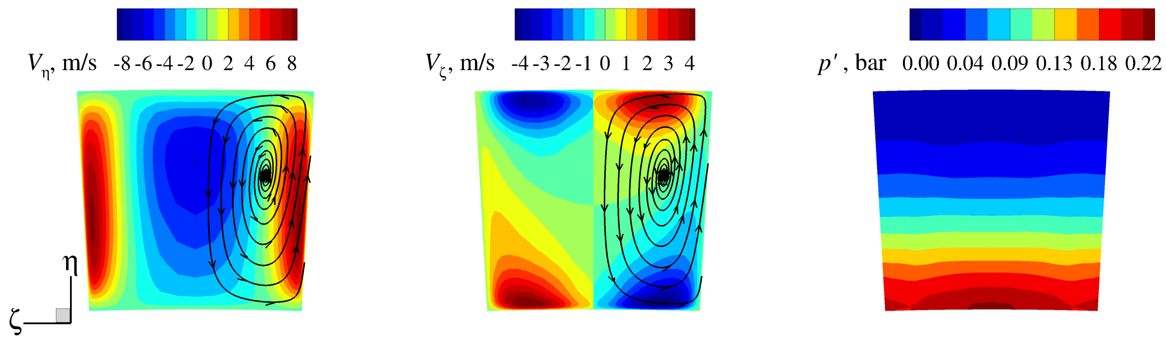

Figure 12: Slice of the channel cross section (fluid domain) in the throat region, showing the secondary motion. The slice is mirrored along the symmetry axis. From left to right: vertical (η direction) and horizontal (ζ direction) tangential velocity components, with streamlines; pressure distribution, $p' = p - p_{min}$.

(5). Indeed, in the initial section of the channel, heat transfer deterioration [37][39] occurs due to the coolant being supercritical at a pressure sufficiently close to the critical one. This phenomenon involves the formation of a low-density layer near the wall, which accelerates more than the high-density core. Consequently, an M-shaped velocity profile arises, leading to the formation of a zero velocity gradient region near the wall that reduces turbulent diffusion and produces thermal insulation at the wall. The scenario is illustrated in Figure 14 for the current case, referring to section (5) of Figure 11. The reduced model does not account for this phenomenon, resulting in a significant underestimation of wall temperature in regions where heat transfer deterioration conditions are met (low mass flux, high heat flux, and bulk temperature below the pseudo-critical value). Despite the discrepancy between the reduced model and CHT simulation, the design objective is achieved as the wall temperature remains below 800 K along the cooling channel, except at the exit, where the initial peak of hot gas side occurs, which is not expected in reality.
For what concerns bulk quantities, Figure 13(b) shows the evolution of bulk pressure and temperature in the channel. The steepest increase in bulk temperature occurs in the throat region, where the maximum heat flux is present. Along the combustion chamber, a linear increase is observed as the heat flux is nearly constant in that region (Figure 13(a)). Regarding the pressure evolution, the design results in a very satisfactory outcome, with a pressure drop of only 2% of the outlet pressure. Critical areas for the pressure loss are the throat region, where the hydraulic diameter is minimum, and the initial segment of the combustion chamber, where the bulk temperature increase has to be counterbalanced by a cross section reduction for effective cooling.
Lastly, a comparison is drawn in Table 1 between the annular configuration proposed by Fiore et al. [16] and the modular configuration presented in this work. The focus of the comparison is on the internal expansion segment of the cooling system. In the annular configuration, a double regenerative circuit is employed, with the outer wall being cooled by liquid oxygen and the inner wall being cooled by liquid methane. Both cooling systems are designed with the same approach to maintain the wall temperature below 800 K. A noticeable difference emerges in the power extracted by the cooling system in the annular setup, which is almost twice that of the modular configuration. This difference arises from higher convective heat transfer (as evidenced by the peak hot gas side heat transfer coefficients listed in the table) and a significantly larger surface area exposed to the hot gas in the annular design. Consequently, the annular configuration necessitates a double regenerative circuit to manage the thermal loads effectively. Moreover, achieving sufficient cooling capability in the annular plug presents a much more critical challenge, which has to be addressed with the adoption of a complex geometry, involving helicoidal channels with high helix angle (up to 70°). Such a design leads to significantly higher pressure drop in the channels for both propellants, being 15 times greater than in the modular configuration. Based on this comparison, the clustered design appears to be a valid choice to mitigate the criticality associated with managing thermal loads in annular aerospike designs.

Configuration		Δp, bar	ΔT_b, K	$h_{g,max}$, kW/(m·K)	$\dot{Q}$, MW
Annular	O2 (outer wall)	36	340	22	10.4
	CH4 (inner wall)	36	380	17.5	9.4
Clustered	CH4	2.3	518	17.5	12.9

Table 1: Comparison of the annular configuration [16] with the modular configuration of the present work. The annular configuration involves a double regenerative circuit: fuel for the inner wall and oxidizer for the outer wall.

DOI: 10.13009/EUCASS2023-670

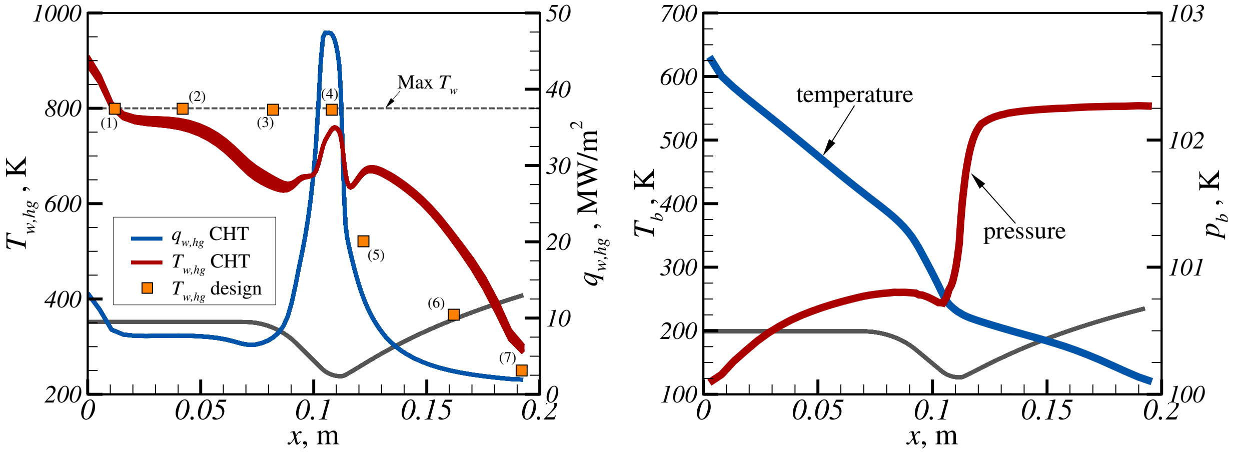

(a) Hot gas side temperature and heat flux.

(b) Bulk pressure and temperature.

Figure 13: Conjugate heat transfer simulation results plotted vs the axial coordinate.

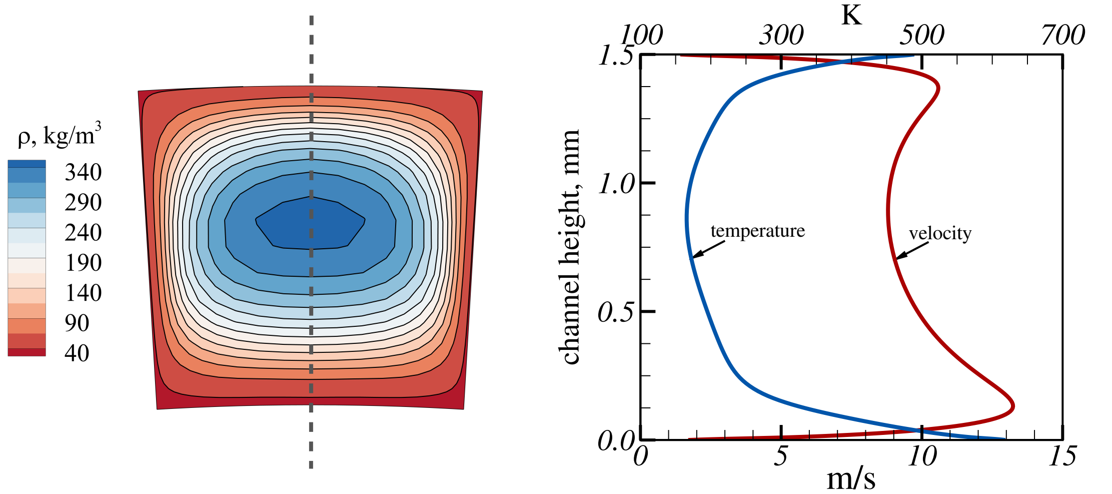

(a) Coolant density contour. Dashed line: symmetry plane.

(b) Coolant temperature and velocity distributions on the symmetry line.

Figure 14: Channel cross section at location (5) of Figure 11. The formation of a low density layer near the wall promotes heat transfer deterioration.

5. Conclusions

This work focused on the assessment of the design of a modular aerospike nozzle cooling system configuration for a 10-ton class LOX/CH4 liquid rocket engine. The use of aerospike nozzles offers potential advantages such as higher expansion ratios and compactness compared to conventional bell nozzles. However, one of the primary challenges with annular aerospike nozzles is the management of thermal loads due to the large surface area exposed to maximum heat flux.

The study of a modular design, which is achieved by a cluster of conventional round bell nozzles arranged around the plug, has been performed through simulations of the hot gas flow within the thrust chamber, and through conjugate heat transfer simulations of the cooling jacket. The analysis has been conducted exploiting both a reduced model, involving heat transfer correlations and simplified heat conduction in the solid, and a comprehensive numerical simulation, able to provide a more accurate assessment of the coolant flow characteristics in the channels. Comparing the conjugate heat transfer solution with the reduced model, significant errors in the evaluation of wall temperature have been observed due to the complex, multi-dimensional phenomena that characterize the coolant flow, such as heat transfer deterioration

DOI: 10.13009/EUCASS2023-670

and secondary flows promoted by channel curvature. However, these discrepancies did not jeopardize the study of the current case since the channel geometry in the most critical location, the throat region, was properly sized.
Overall, the modular aerospike nozzle configuration shows promise in addressing the thermal management challenges associated with annular aerospike nozzles. It allows the realization of a simpler cooling system geometry, with a fixed number of axial channels, as no bifurcations or helicoidal arrangements are needed to achieve proper cooling. As a result, pressure losses are largely reduced, and the modular configuration offers a potential solution for this specific application.

References

[1] K. Berman and F. W. Crimp, "Performance of plug-type rocket exhaust nozzles," *ARS Journal*, vol. 31, no. 1, pp. 18–23, 1961.

[2] J. F. Connors, R. W. Cubbison, and G. A. Mitchell, "Annular internal-external-expansion rocket nozzles for large booster applications," *NASA Technical Report TN D-1049*, 1961.

[3] F. Nasuti and M. Onofri, "Methodology to solve flowfields of plug nozzles for future launchers," *Journal of Propulsion and Power*, vol. 14, no. 3, pp. 318–326, 1998.

[4] H. Immich, F. Nasuti, M. Onofri, and M. Caporicci, "Experimental and numerical analysis of linear plug nozzles," in *8th AIAA International Space Planes and Hypersonic Systems and Technologies Conference, AIAA Paper 1998-1603*, 1998.

[5] M. Onofri, M. Calabro, G. Hagemann, H. Immich, P. Sacher, F. Nasuti, and P. Reijasse, "Plug nozzles: summary of flow features and engine performance - Overview of RTO/AVT WG 10 subgroup 1," in *40th AIAA Aerospace Sciences Meeting & Exhibit, AIAA Paper 2002-584*, 2002.

[6] C. A. Aukerman, "Plug nozzles-the ultimate customer driven propulsion system," *NASA Contractor Report CR-187169*, 1991.

[7] G. Hagemann, A. Preuss, J. Kretschmer, F. Grauer, M. Frey, R. Ryden, and R. Stark, "Technology investigation for high area ratio nozzle extensions," in *39th AIAA/ASME/SAE/ASEE Joint Propulsion Conference and Exhibit, AIAA Paper 2003-4912*, 2003.

[8] J. Hall, C. Hartsfield, J. Simmons, and R. Branam, "Optimized dual-expander aerospike nozzle upper stage rocket engine," in *49th AIAA Aerospace Sciences Meeting including the New Horizons Forum and Aerospace Exposition, AIAA Paper 2011-419*, 2011.

[9] F. Nasuti, M. Fiore, V. Messina, A. Valeriani, and D. Bianchi, "Design and evaluation of aerospike nozzles for an upper stage application," in *Space Propulsion 2021, 17-19 March 2021*, 2021.

[10] T. Ito and K. Fujii, "Numerical analysis of the base bleed effect on the aerospike nozzles," *40th AIAA Aerospace Sciences Meeting & Exhibit, AIAA Paper 2002-0512*, 2002.

[11] F. Nasuti and M. Onofri, "Theoretical analysis and engineering modeling of flowfields in clustered module plug nozzles," *Journal of Propulsion and Power*, vol. 15, no. 4, pp. 544–551, 1999.

[12] F. Rossi, G. Esnault, Z. Sápi, N. Palumbo, A. Argemi, and R. Bergström, "Research activities in the development of Demo P1: a LOX/LNG aerospike engine demonstrator," in *Space Propulsion 2021, 17-19 March 2021*, 2021.

[13] F. Rossi, Z. Sápi, N. Palumbo, A. Demediuk, and M. Ampudia, "Manufacturing and hot-fire test campaign of the DemoP1 aerospike engine demonstrator," in *Space Propulsion 2022, Estoril, Portugal, 9-13 May 2022*, 2022.

[14] G. Esnault and F. Rossi, "Design and CFD analysis of the LOX/LCH4 dual regenerative cooling circuit of the DemoP1 Demonstrator," in *Aerospace Europe Conference, Warsaw, Poland, 23-26 November 2021*, 2021.

[15] F. Kerstens, A. Cervone, and P. Gradl, "End to end process evaluation for additively manufactured liquid rocket engine thrust chambers," *Acta Astronautica*, vol. 182, pp. 454–465, 2021.

[16] M. Fiore, A. Sereno, D. Bianchi, and F. Nasuti, "Cooling system design for an upper-stage aerospike," in *International Symposium on Space Technology and Science 2023, 3-9 June 2023 Kurume, Japan*, 2021.

DOI: 10.13009/EUCASS2023-670

[17] D. K. Huzel and D. H. Huang, *Modern engineering for design of liquid-propellant rocket engines*. AIAA, 1992, vol. 147.

[18] P. R. Spalart and S. R. Allmaras, "A One-Equation Turbulence Model for Aerodynamic Flow," *La Recherche Aerospatiale: Bulletin Bimestriel de lOffice National dEtudes et de Recherches Aerospatiales*, no. 1, pp. 5–21, 1994.

[19] B. Betti, D. Bianchi, F. Nasuti, and E. Martelli, "Chemical Reaction Effects on Heat Loads of CH4/O2 and H2/O2 Rockets," *AIAA Journal*, vol. 54, no. 5, pp. 1693–1703, 2016.

[20] W. Jones and R. Lindstedt, "Global reaction schemes for hydrocarbon combustion," *Combustion and Flame*, vol. 73, no. 3, pp. 233–249, 1988. [Online]. Available: https://www.sciencedirect.com/science/article/pii/0010218088900211

[21] F. Lockwood and N. Shah, "A new radiation solution method for incorporation in general combustion prediction procedures," *Symposium (International) on Combustion*, vol. 18, no. 1, pp. 1405–1414, 1981, eighteenth Symposium (International) on Combustion. [Online]. Available: https://www.sciencedirect.com/science/article/pii/S0082078481801440

[22] G. Leccese, D. Bianchi, B. Betti, D. Lentini, and F. Nasuti, "Convective and radiative wall heat transfer in liquid rocket thrust chambers," *Journal of Propulsion and Power*, vol. 34, no. 2, pp. 318–326, 2018.

[23] P. Concio, M. Tindaro Migliorino, D. Bianchi, and F. Nasuti, "Numerical estimation of nozzle throat heat flux in oxygen-methane rocket engines," *Journal of Propulsion and Power*, vol. 39, no. 1, pp. 71–83, 2023.

[24] P. R. Gradl, C. S. Protz, D. L. Ellis, and S. E. Greene, "Progress in additively manufactured copper-alloy GRCop-84, GRCop-42, and bimetallic combustion chambers for liquid rocket engines," in *International Astronautical Congress (IAC)*, no. IAC-19. C4. 3.5 x52514, 2019.

[25] C. Zeng, H. Wen, B. C. Bernard, J. R. Raush, P. R. Gradl, M. Khonsari, and S. Guo, "Effect of temperature history on thermal properties of additively manufactured C-18150 alloy samples," *Manufacturing Letters*, vol. 28, pp. 25–29, 2021.

[26] I. H. Bell, J. Wronski, S. Quoilin, and V. Lemort, "Pure and pseudo-pure fluid thermophysical property evaluation and the open-source thermophysical property library coolprop," *Industrial & Engineering Chemistry Research*, vol. 53, no. 6, pp. 2498–2508, 2014. [Online]. Available: http://pubs.acs.org/doi/abs/10.1021/ie4033999

[27] D. F. Dipprey and R. H. Sabersky, "Heat and momentum transfer in smooth and rough tubes at various Prandtl numbers," *International Journal of Heat and Mass Transfer*, vol. 6, no. 5, pp. 329–353, 1963.

[28] M. Pizzarelli and F. Battista, "Oxygen-methane rocket thrust chambers: Review of heat transfer experimental studies," *Acta Astronautica*, vol. 209, pp. 48–66, 8 2023.

[29] M. Niino, A. Kumakawa, N. Yatsuyanagi, and A. Suzuki, "Heat transfer characteristics of liquid hydrogen as a coolant for the LO2/LH2 rocket thrust chamber with the channel wall construction," *18th Joint Propulsion Conference*, 1982.

[30] M. Fagherazzi, M. Santi, F. Barato, and M. Pizzarelli, "A simplified thermal analysis model for regeneratively cooled rocket engine thrust chambers and its calibration with experimental data," *Aerospace*, vol. 10, 5 2023.

[31] C. K. Stimpson, J. C. Snyder, K. A. Thole, and D. Mongillo, "Scaling roughness effects on pressure loss and heat transfer of additively manufactured channels," *Journal of Turbomachinery*, vol. 139, no. 2, 2017.

[32] M. Fagherazzi, M. Santi, F. Barato, and D. Pavarin, "Design and testing of a 3d printed regenerative cooled nozzle for a hydrogen peroxide based bi-propellant thruster," in *AIAA Propulsion and Energy 2021 Forum, August 9-11*, 2021.

[33] M. Pizzarelli, F. Nasuti, and M. Onofri, "Coupled wall heat conduction and coolant flow analysis for liquid rocket engines," *Journal of Propulsion and Power*, vol. 29, no. 1, pp. 34–41, 2013.

[34] P. Spalart and S. Allmaras, "A one-equation turbulence model for aerodynamic flows," in *30th aerospace sciences meeting and exhibit*, 1992, p. 439.

DOI: 10.13009/EUCASS2023-670

[35] B. Aupoix and P. Spalart, “Extensions of the spalart–allmaras turbulence model to account for wall roughness,” *International Journal of Heat and Fluid Flow*, vol. 24, no. 4, pp. 454–462, 2003.

[36] M. Pizzarelli, F. Nasuti, R. Paciorri, and M. Onofri, “Numerical analysis of three-dimensional flow of supercritical fluid in cooling channels,” *AIAA Journal*, vol. 47, no. 11, pp. 2534–2543, Nov. 2009.

[37] M. Pizzarelli, A. Urbano, and F. Nasuti, “Numerical analysis of deterioration in heat transfer to near-critical rocket propellants,” *Numerical Heat Transfer, Part A: Applications*, vol. 57, no. 5, pp. 297–314, 2010.

[38] M. Pizzarelli, F. Nasuti, and M. Onofri, “Analysis of curved-cooling-channel flow and heat transfer in rocket engines,” *Journal of Propulsion and Power*, vol. 27, no. 5, pp. 1045–1053, 2011.

[39] M. Pizzarelli and F. Nasuti, “Pseudo-boiling and heat transfer deterioration while heating supercritical liquid rocket engine propellants,” *Journal of Supercritical Fluids*, vol. 168, 2 2021.